MMIC GaAs Isolators and Quasi-Circulators With Co-Designed RF Filtering Functionality

ANDREA ASHLEY ®[1] (Member, IEEE) AND DIMITRA PSYCHOGIOU ®[2,3] (Senior Member, IEEE)

(Regular Paper)

[1]Department of Electrical, Computer, and Energy Engineering, University of Colorado Boulder, Boulder, CO 80309 USA
[2]School of Engineering, University College Cork, T12 K8AF Cork, Ireland
[3]Tyndall National Institute, T12 R5CP Cork, Ireland

CORRESPONDING AUTHOR: Dimitra Psychogiou (e-mail: dpsychogiou@ucc.ie).

ABSTRACT This paper reports on the RF design and practical development of GaAs MMIC multi-functional RF isolators and quasi-circulators with embedded filtering functionality. They are based on cascaded arrays of non-reciprocal resonators (NRRs), passive resonators, and impedance inverters. A unique transistor-based architecture is used for the realization of the NRR that exhibits an one-pole type bandpass response in the forward direction and RF signal cancellation in the reversed one. By controlling the number and type of resonators within cascaded resonator arrays, different levels of gain, out-of-band selectivity and in-band isolation can be obtained. The operating principles of the multi-functional isolator/filtering and quasi-circulator/filtering concepts are presented through synthesized and linear circuit-simulated examples. Practical design aspects using a commercially available GaAs MMIC process are also discussed. For proof-of-concept demonstration purposes, four prototypes were designed and experimentally validated at X-band. They include: i) a NRR, ii) a two-resonator based frequency selective isolator (FSI), iii) a five-resonator based FSI, and iv) a two-pole/two-TZ frequency selective quasi-circulator (FSQC).

INDEX TERMS Bandpass filter, circulator, integrated circuit, isolator, miniaturization, MMIC filter, non-reciprocal filter, quasi-circulator, RF co-design.

I. INTRODUCTION

Miniaturized RF transceivers are increasingly needed in wireless and radar communications [1], [2]. While miniaturization has been primarily focused on the antenna interface [3], [4], [5] and the active devices (i.e., low-noise amplifier, power amplifier) [6], [7], [8] of the RF transceiver, their size is often dictated by the off-chip components, such as the circulators, isolators and the RF bandpass filters (BPFs) [9], [10], [11], [12], [13]. Conventional ferrite-based circulators and isolators provide good insertion loss (IL) levels (IL < 1 dB in [9]), wide bandwidth and high isolation (IS) (IS > 50 dB [10]), and do not consume any power. However, they are too large to be integrated with the rest of the on-chip components [9], [10], [12], [13]. Furthermore, when passive BPFs are realized with IC-based resonators, they exhibit high levels of IL

(IL ∼ 4.5–9.3 dB in [14], [15]). To reduce the size of the non-reciprocal devices and BPFs, two major miniaturization approaches have been investigated: i) the integration of the non-reciprocal components into a chip using MMIC, CMOS, SiGe, technologies [16], [17], [18], [19], [20], [21], [22], [23], [24], [25], [26], [27], [28], [29] and ii) the RF co-design of the non-reciprocal components with the BPFs with or without ferrite-based elements [31], [32], [33], [34], [35], [36], [37], [38], [39], [40], [41], [42], [43], [44].

Magnetless RF isolators and circulators are typically based on transistor-based circuits [16], [17], [18], [19], [20], [21], [22], [23], [24], [25], [26], [27], [28], [29] that exploit the inherent unilateral behavior of transistors. Example configurations include the combination of a directional coupler and a non-reciprocal transistor-based element in [16], [17],

the series cascade of a low-noise amplifier and an attenuator [18], and the parallel combination of a common-base and a common-collector transistor in [19]. While the isolator in [16] can theoretically achieve infinite levels of IS, its IS depends on the manufacturing tolerances. Furthermore, its size is somewhat large for an integrated isolator (0.054λ by 0.052λ vs. 0.004λ by 0.003λ in [18]). The combination of the LNA and attenuator in [18] exhibits a very small physical size (0.004λ by 0.003λ), however it has high IL. Despite using an LNA (meant to provide enhanced power transmission), the prototype results in 2.5 dB of IL. While some of the circulator topologies exhibit gain in the forward direction [21], [22], [27], [28], [29], [30], not all are matched at the input/output RF ports [23], [24], [25], [28]. Furthermore, all of the aforementioned configurations [16], [17], [18], [19], [20], [21], [22], [23], [24], [25], [26], [27], [28], [29], [30], aren't frequency selective and therefore their corresponding RF front-ends require additional BPFs to cancel out the unwanted RF signals. In addition, the circulators in [25] and [29], [[30] exhibit poor linearity with the their 1-dB compression point (P1dB) being less than -2 dBm. The circulator in [45] demonstrates good linearity, however it isn't IC integrated and only covers frequencies up to 3.56 GHz.

In yet another magnetless circuit-based design approach, spatiotemporally modulated (STM) switched capacitor arrays, transmission lines or resonator-arrays are employed within a three-port network to achieve non-reciprocity [46], [47], [48], [49]. Alternative integration schemes using PCB ([32], [33], [34], [35], [36], [37], [38], [39], [40], [41], [48]) and CMOS based integration platforms ([46], [47], [48], [49]) have been demonstrated. However, the operating principles of many of them have been demonstrated at frequencies <1.2 GHz (e.g., [32], [33], [34], [35], [36], [37], [40], [41], [48], [49]). High-frequency implementations of STM-based circulators using CMOS technologies have also been shown to higher frequencies as for example at 6 GHz in [50], at 28 GHz in [51] and at 60 GHz in [52].

The second miniaturization technique is based on the combination of the function of the isolator/circulator with the function of the BPF into a single device [31], [32], [33], [34], [35], [36], [37], [38], [39], [40], [41], [42], [43], [44]. Using this method, either the BPF or the isolator/circulator can be removed from the RF front-end. Notable demonstrations include: i) the combination of a BPF and a ferrite-based circulator (BPFC) in [31], ii) STM-based non-reciprocal BPFs (NBPFs) in [32], [33], [34], [35], [36], [37], [38], [39], [40], [41], iii) transistor-based NBPFs in [42], [43] and iv) transistor-based co-designed BPFs and quasi-circulators in [44]. While the ferrite-based BPFC in [31] was further miniaturized by capacitively loading its ferrite disk and by reconfiguring its transfer function, it exhibits moderate IL (2.7–4.5 dB) and cannot be integrated in an IC platform due to the presence of the external magnetic biasing. STM NBPFs become non-reciprocal by modulating their resonators using varactors or MEMS [32], [33], [34], [35], [36], [37],

[38], [39], [40], [41]. Nevertheless, they have only been demonstrated for frequencies <1.2 GHz and exhibit high IL (>4.5 dB in [35], [36], [37]) and non-linearities. Transistor-based NBPFs and BPFs/quasi-circulators [42], [43], [44] have enhanced power transmission (gain >2.8 dB in [43]) and moderate-to-high levels of IS in the reverse direction (44 dB in [42]). However, only one of these topologies has been MMIC implemented.

Considering the aforementioned limitations, this manuscript discusses for the first time the design and practical development of a new class of fully-integrated frequency-selective isolators (FSIs) and quasi-circulators (FSQCs) within an MMIC integration platform alongside their coupled-resonator-based modeling. These new multi-functional devices aim to decrease the size of the RF transceiver through: i) the co-design of BPFs and isolators/circulators and ii) their integration in a MMIC platform. The proposed concept is designed to operate at X-band and implemented on a commercially available GaAs MMIC process. It is based on cascading non-reciprocal resonators (NRRs) with either passive microwave resonators and/or a transmission zero (TZ) generation cell. Therefore, the devised FSI/FSQC can be designed for various transfer functions with varying levels of IS and frequency selectivity depending on the type and the number of resonators that are incorporated in the topology. A detailed design methodology using coupled-resonator-based filter design techniques is uniquely demonstrated in this work for MMIC-based FSIs and FSQCs allowing for modular and scalable design that can be tailored to high order filtering transfer functions.

The content of this paper is organized as follows. Section II, discusses the operating principles and practical implementation in a MMIC GaAs process of the NRR and the FSI/FSQC. In Section III, the experimental testing of the GaAs prototypes at X-band is presented. They include: a NRR, a two-resonator FSI, a five-resonator FSI, and a two-pole/two-TZ FSQC. Lastly, the main contributions of the paper are summarized in Section IV.

II. DESIGN PRINCIPLES
This section discusses the RF design and operating principles of the fully-integrated FSI/FSQC concept. It starts by introducing the NRR concept and its practical implementation using a commercially available GaAs MMIC process and continues with its use in the FSI/FSQC through synthesized and circuit-based examples.

A. NON-RECIPROCAL RESONATOR
The circuit details of the NRR are provided in Fig. 1. It comprises two main parallel RF signal paths: i) a transistor-based path shaped by resistors and capacitors and ii) a capacitively-loaded transmission line (TL). The transistor-based path is designed to have gain in the forward direction and isolation in the reverse direction as seen in Fig. 1(b). The capacitively-loaded TL is added in parallel to counterbalance the phase of
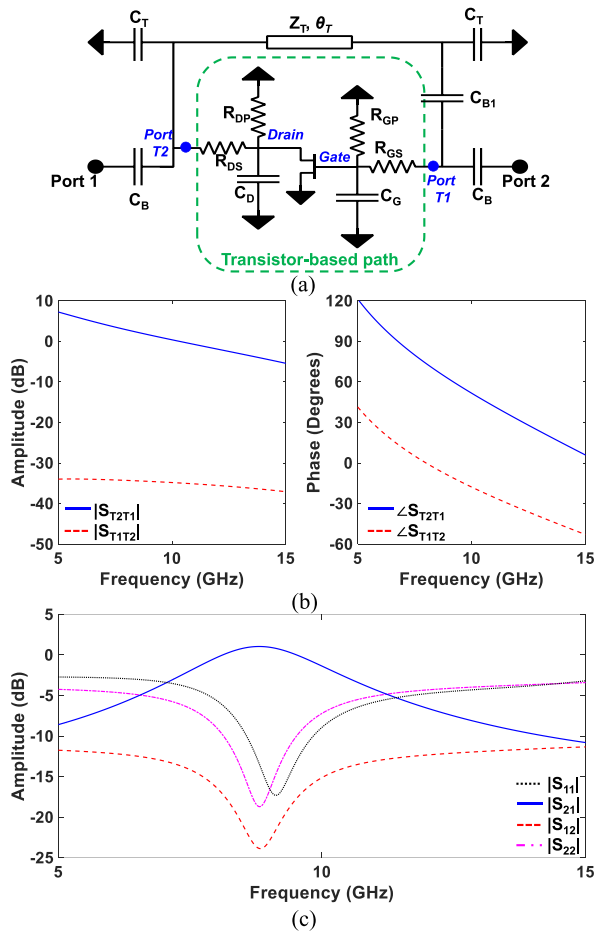
(a)

(b)

(c)

FIGURE 1. NRR. (a) Circuit schematic with the transistor-based path circled in green, (b) Magnitude and phase responses for the transistor-based path, and (c) Circuit-simulated response for the circuit in (a). the component values are as follows: $R_{GS} = 45.1\,\Omega$, $R_{GP} = 23.6\,\Omega$, $R_{DS} = 10.1\,\Omega$, $R_{DP} = 770\,\Omega$, $C_G = 0.78$ pF, $C_D = 0.19$ pF, $C_B = 3.1$ pF, and $C_{B1} = 6.0$ pF. The transistor used in the NRR is an 8-finger pHEMT.

(a)   (b)

FIGURE 2. Design studies varying the bias point of the 8-finger pHEMT transistor. (a) V_G. (b) V_D. When not being altered, $V_G = 0.8$ V and $V_D = 2$ V.

(a)   (b)

(c)   (d)

FIGURE 3. k and $B1$ as a function of: (a) R_{GS}, (b) R_{GP}, (c) R_{DS}, (d) R_{DP}. When not being altered: $R_{GS} = 45.1\,\Omega$, $R_{GP} = 23.6\,\Omega$, $R_{DS} = 10.1\,\Omega$, and $R_{DP} = 770\,\Omega$.

the transistor-based path and create the non-reciprocal resonance [see Fig. 1(c)].

To illustrate the operating principles of the NRR, the overall design process is presented by first specifying the transistor, which is set in a common source configuration, (i.e., looking into the gate and the drain of the transistor in Fig. 1(a)) and its bias point so that the NRR can exhibit gain at the design frequency. It should be noticed that its gain and IS are affected by the bias point [see Fig. 2].

In order to create the transistor-based path, resistors and capacitors are placed at the gate and drain of the transistor. The resistors facilitate a non-reciprocal response that maintains gain at the design frequency and unconditional stability (stability factor $k > 1$ and auxiliary stability factor $B1 > 0$) over the entire frequency range. The capacitors are added to provide control over the frequency at which the maximum gain, the maximum IS and the best matching for both the input and output ports occurs. As seen in Fig. 1(b), the transistor-based path exhibits a positive phase response in the
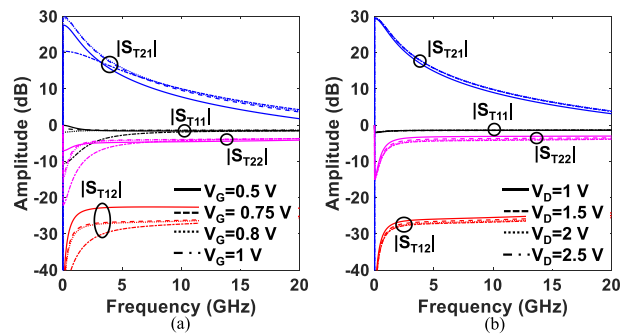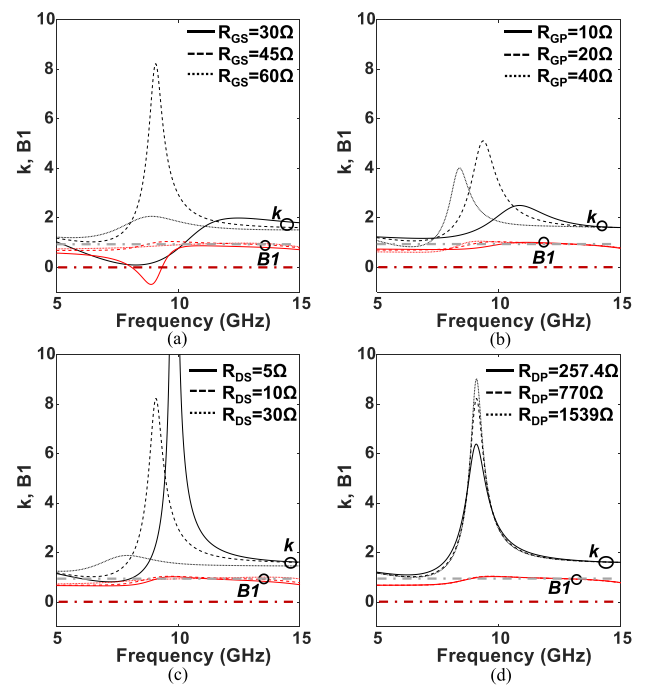
forward direction, which is approximately 64° at the design frequency. When the TL with equal but opposite phase of the transistor-based path is added in parallel, the circuit in Fig. 1(a) results in a resonance at the design frequency [see Fig. 1(c)] as also discussed in [42]. For this particular NRR, the TL was capacitively-loaded to reduce the overall size of the transmission line.

To better demonstrate how some of the components in the transistor-based path affect the overall performance of the NRR, some design studies are considered and are provided in Figs. 3 and 4. As it can be seen in Fig. 3(a), R_{GS} primarily affects the unconditional stability of the NRR; in particular, when R_{GS} is decreased to 30 Ω, the conditions $k > 1$ and $B1 > 0$ are no longer satisfied. The gate and drain capacitances (C_G and C_D) were also altered to see how their values affect the
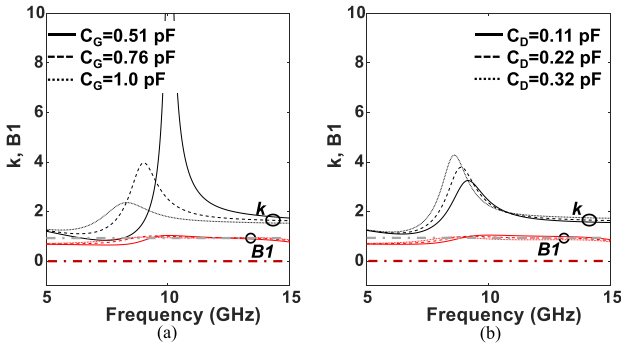
FIGURE 4. k and $B1$ as a function of the gate capacitance (C_G) and the drain capacitance (C_D). (a) C_G. (b) C_D. When not being varied, $C_G = 0.78$ pF and $C_D = 0.19$ pF.

FIGURE 6. CRD and synthesized response for the NRR in Fig. 1(a) using the coupling element values in Table 1.
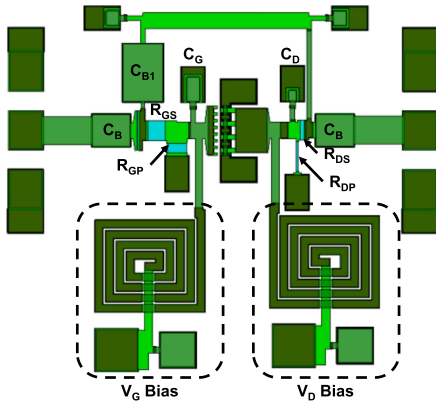

FIGURE 5. Layout of the MMIC NRR in Fig. 1(a). Green layers: metal, blue: resistive layer. The component values are as follows: $R_{GS} = 45.1\Omega$, $R_{GP} = 23.6\Omega$, $R_{DS} = 10.1\Omega$, $R_{DP} = 770\Omega$, $C_G = 0.78$ pF, $C_D = 0.19$ pF, $C_B = 3.1$ pF, and $C_{B1} = 6.0$ pF.

TABLE 1. M-and R-Matrix Element Values for the CRD in Fig. 6

$M_{01}=M_{12}=M_{34}=M_{45}$	1
M_{23}	-0.0153-j0.0292
M_{32}	1.4739-j1.5239
M_{14}	2.6895+j0.0614
$R_{00}=R_{55}$	1
R_{11}	0.1075-j0.019
R_{22}	1.07-j0.0814
R_{33}	0.6328-j0.5082
R_{44}	0.1217-j1.1335

overall stability of the NRR and are provided in Fig. 4. As it can be seen, the stability (i.e., k) is slightly affected by C_G.

A layout for the circuit showing all of the individual components in Fig. 1(a) is provided in Fig. 5. This implementation uses a capacitively-loaded TL for compactness and has a blocking capacitor in the path to prevent bias leakage. In order to properly bias the gate and the drain of the transistor, high impedance inductors were utilized. The inductors were used to conserve space and do not add significant loss to the overall system. The circuit-simulated S-parameters for the NRR, when biased at $V_D = 2V$, $V_G = 0.8V$, are provided in Fig. 1(c), resulting in 1.0 dB of gain and 24.9 dB of IS at 8.9 GHz. It is worth noting that the fractional bandwidth (FBW), which is 30.6% for this case, is predetermined by the design parameters of the NRR and can't be altered.

B. NRR MODELING USING COUPLING ROUTING DIAGRAMS

Since the NRR creates a single pole type of transfer function in the forward direction and a TZ in the reverse one, it can be represented by the coupling routing diagram (CRD) and
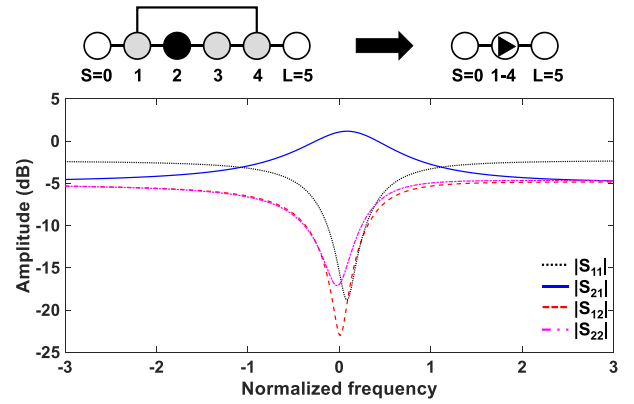
its synthesized response in Fig. 6. In particular, the transistor-based path is represented by the couplings between nodes 1, 2, 3 and 4 (i.e., M_{12}, M_{23}, M_{32}, and M_{34}) while the capacitively loaded TL-based path is represented by the coupling between nodes 1 and 4 (i.e., M_{14}). It should be noted that different coupling element values are used for the coupling between nodes 2 and 3 in order to generate the desired non-reciprocal S-parameters. The coupling element values have been calculated using the design method in [42] and are summarized in Table 1. Specifically, the coupling between nodes 1 and 2 and 3 and 4 are set arbitrarily to 1. Next, the couplings between nodes 2 and 3 (M_{23} and M_{32}) and their associated R-matrix values (R_{22} and R_{33}) are calculated. In this case, the Y-parameters of the transistor-based path (Y_{21}, Y_{12}, Y_{11}, and Y_{22}) are considered. In particular, M_{23}, M_{32}, R_{22}, and R_{33} are calculated using (1), where Y'_{21}, Y'_{12}, Y'_{11}, and Y'_{22} are the scaled Y-parameters of the transistor-based path. Y'_{11}, Y'_{21}, Y'_{12}, and Y'_{22} are defined using (2)–(3).

$$M_{23} = \frac{50}{Y'_{12}}; M_{23} = \frac{50}{Y'_{21}}; \ R_{22} = 50Y'_{11}; \ R_{33} = 50Y'_{22} \quad (1)$$

$$Y'_{11} = \frac{-jY_{22}}{Y_{21}Y'_{21}}; Y'_{21} = j2500\left(Y_{12} - \frac{Y_{11}Y_{22}}{Y_{21}}\right) \quad (2)$$
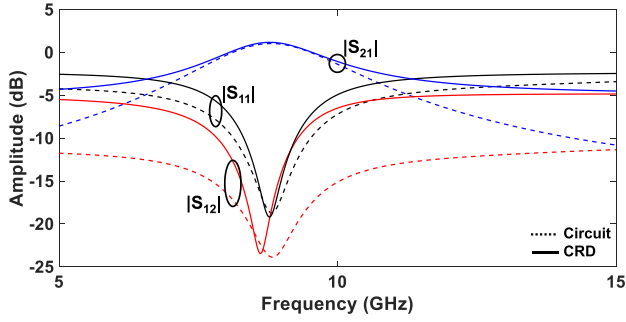
FIGURE 7. Comparison of CRD-synthesized response using the coupling element values in Table 1 and circuit-simulated response of the NRR in Fig. 1(a).

$$Y_{22}' = \frac{-jY_{11}}{Y_{21}Y_{21}'}; \ Y_{12}' = \frac{-50}{j/50Y_{21} + 50Y_{11}'Y_{22}'Y_{21}'} \quad (3)$$

$$R_{11} = 50Y_{TL11}; \ R_{44} = 50Y_{TL22} \quad (4)$$

Finally, the coupling between nodes 1 and 4 (M_{14}) is obtained using the normalized admittance of the capacitively-loaded TL. Since the phase of the capacitively-loaded TL is not exactly 90° at the design frequency, the R-matrix values for node 1, 4 R_{11} and R_{44} are found using (4), where Y_{TL11} and Y_{TL22} are the admittance of the input and output ports of TL-based path, respectively. Having specified the M- and the R-matrix element values of the NRR, its S-parameters can be calculated by (5)–(7).

$$S_{11} = -1 + 2 (R + sU - jM)^{-1}_{N+2,N+2} \quad (5)$$

$$S_{21} = 2 (R + sU - jM)^{-1}_{1,N+2} \quad (6)$$

$$S_{12} = 2 (R + sU - jM)^{-1}_{N+2,1} \quad (7)$$

A comparison of the CRD-synthesized response and the circuit-simulated response are provided in Fig. 7. As it can be seen, the CRD lines up well with the circuit-simulated response at the design frequency, thus validating the proposed CRD model. The variances between the CRD response and the circuit-simulated response outside of the design frequency are due to the CRD only being applicable to a single frequency.

C. FREQUENCY SELECTIVE ISOLATOR

In order to create a frequency selective isolator (FSI), the NRR can be cascaded through impedance inverters (i.e., quarter-wavelength long TLs at f_{cen}) with alternative resonator types to achieve different types of transfer functions. In particular, when the NRR is cascaded with additional NRRs, the order of the FSI, its gain, and IS are increased. If the NRR is combined with passive microwave resonators, the frequency selectivity of the FSI is increased, however the gain and IS levels are the same as in the NRR case when using ideal (i.e., lossless) passive resonators. Examples of these characteristics are provided in the CRD-synthesized examples of a two-resonator FSI in Fig. 8 and a five-resonator FSI in Fig. 9.
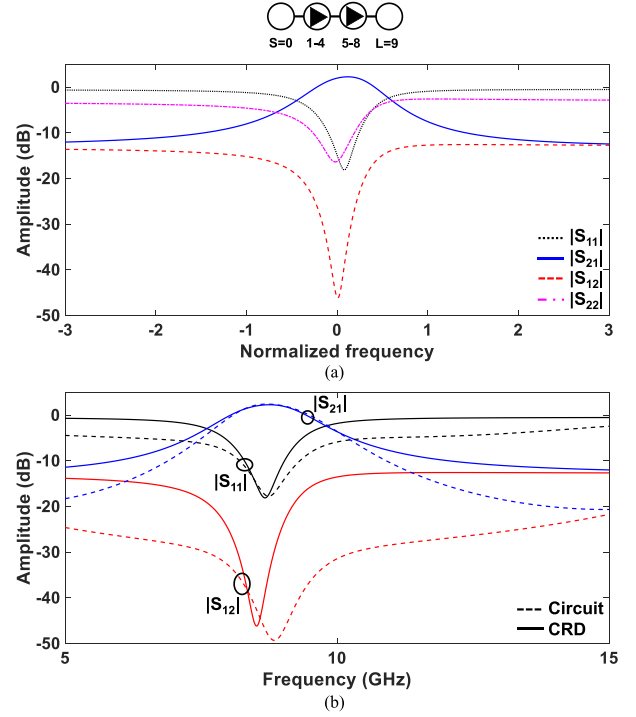

FIGURE 8. (a) Simplified CRD and normalized frequency response for the second order FSI. (b) Comparison of the CRD-synthesized response and circuit-simulated response. The coupling element values are as follows: $M_{01} = M_{12} = M_{34} = M_{45} = M_{56} = M_{78} = M_{89} = 1$, $M_{23} = M_{67} = -0.0153-j0.0292$, $M_{32} = M_{76} = 1.4739-j1.5239$, and $M_{14} = M_{58} = 2.6895+j0.0614$.
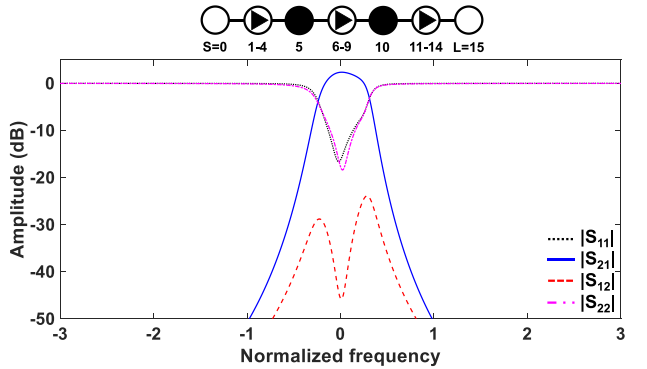

FIGURE 9. Simplified CRD and normalized frequency response for the fifth order FSI. The coupling values are as follows: $M_{01} = M_{12} = M_{56} = M_{67} = M_{1011} = M_{1112} = 0.417$, $M_{23} = M_{45} = M_{78} = M_{910} = 1$, $M_{34} = M_{89} = -0.0153-j0.0292$, $M_{43} = M_{98} = 1.4739-j1.5239$, and $M_{25} = M_{710} = 2.6895+j0.0614$.

Specifically, the two-resonator FSI in Fig. 8 is comprised of two NRRs that are coupled through an impedance inverter (M_{45}) equal to 1. In addition, a comparison of the CRD-synthesized response and the circuit-simulated response is provided in Fig. 8(b). Similar to the NRR, the variance in the two responses is due to the CRD only being applicable to a single frequency. The block diagram and CRD-synthesized response for the five-resonator FSI is presented in Fig. 9
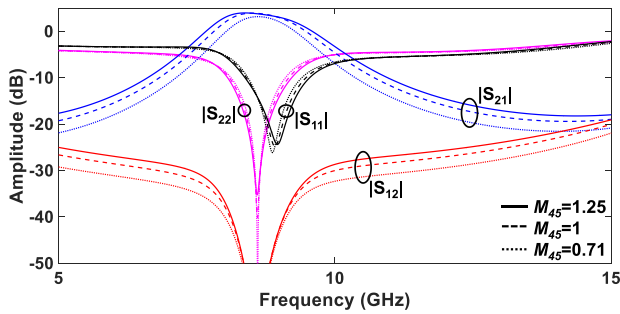
FIGURE 10. Varying the BW of the two-resonator FSI through M_{45}.

TABLE 2. Comparison of the NRR and FSIs in Fig. 11

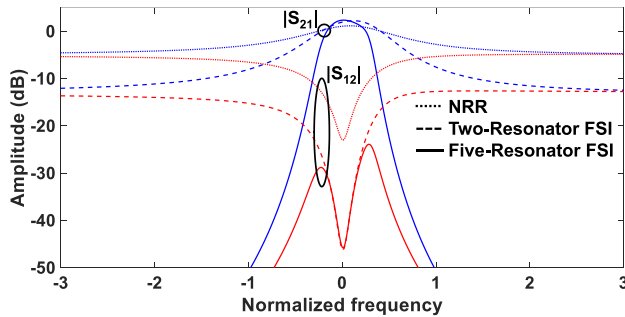| Topology	$|S_{21}|$	$|S_{12}|$
NRR	+1.1	-23
Two-Resonator FSI	+2.2	-46
Five-Resonator FSI	+2.2	-46

FIGURE 11. Comparison of $|S_{21}|$ and $|S_{12}|$ for the NRR, the two-resonator FSI, and the five-resonator FSI.

and is comprised of two NRRs and three passive microwave resonators. The coupling values for the inverters in the five-resonator FSI are as follows: $M_{01} = M_{12} = M_{56} = M_{67} = M_{1011} = M_{1112} = 0.417$. Unlike in the NRR, the BW of the FSIs can be controlled through the impedance inverters. An example demonstrating this operating principle for the two-resonator FSI is shown in Fig. 10. As it can be seen, as the coupling value of the impedance inverter connecting the two FSIs (M_{45}) is decreased, the BW of the FSI is decreased. A comparison between the NRR, two-resonator FSI, and the five-resonator FSI, is provided in Table 2 and Fig. 11. The two-resonator FSI and the five-resonator FSI have comparable gain and isolation levels due to having two NRRs present in the filter topology, however the frequency selectivity of the five-resonator FSI is higher. While a finite number of examples have been demonstrated, a wide range of transfer functions could be implemented by altering the number of the NRRs and the passive resonators in the filter topology. Furthermore, it is worth noting that while stability has only

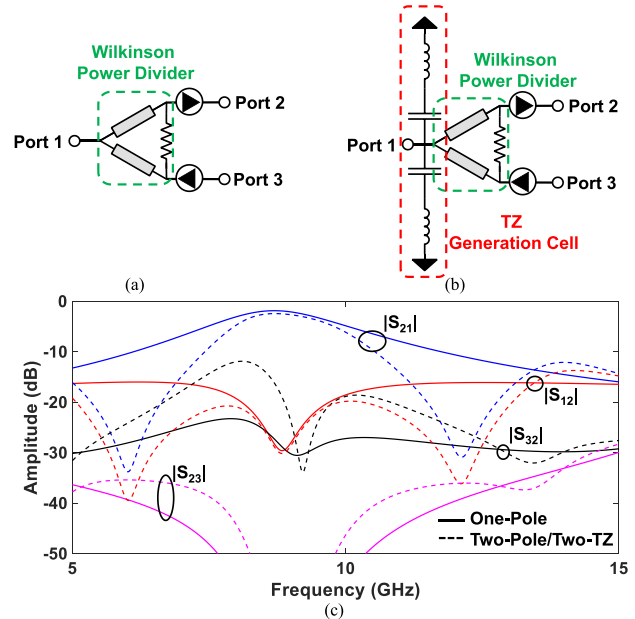**FIGURE 12.** Layout of the proposed fifth order FSI.

FIGURE 13. Conceptual block diagrams for the: (a) One-pole FSQC and (b) the two-pole/two-TZ FSQC. (c) Circuit-simulated S-parameters for the one-pole and the two-pole/two TZ FSQCs. The wilkinson power divider is circled in green and the TZ generation cell is circled in red.

been presented for a single NRR, all of the presented FSIs are unconditionally stable.

In order to practically realize the FSIs using the MMIC platform, the design begins by using the NRR layout in Fig. 5. Afterwards, the impedance inverters are materialized through quarter wavelength long TLs at the design frequency. Since the NRRs require biasing, blocking capacitors are incorporated to prevent leakage to the RF ports. Finally, the passive resonators are realized through shorted quarter-wavelength long stubs to provide low loss and small size. The layout for the five-resonator FSI is provided in Fig. 12.

D. FREQUENCY SELECTIVE QUASI-CIRCULATORS

The NRR concept can also be expanded to the realization of three-port networks, such as frequency selective quasi-circulators (FSQCs) as shown in the conceptual diagrams (Fig. 13(a), (b)) and circuit-simulated responses in Fig. 13(c). The most basic form of the FSQC is shown in Fig. 13(a) and it exhibits a one-pole type transfer function, as demonstrated in Fig. 13(c). The FSQC consists of a Wilkinson power divider at the input port and a NRR (which contributes to one pole per path) at each output port (port 2 and 3) to enable the signal to flow in a single direction and provide IS in the reverse
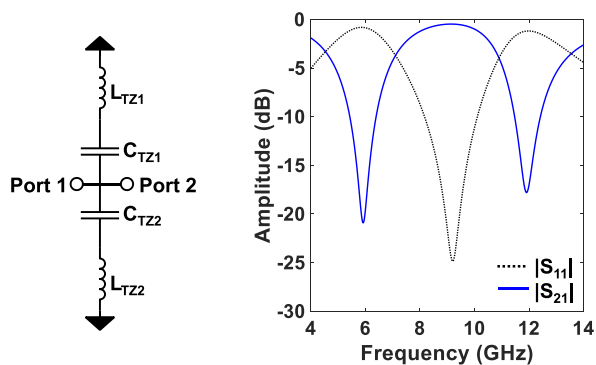
FIGURE 14. Circuit diagram and circuit-simulated response of the TZ generation cell.
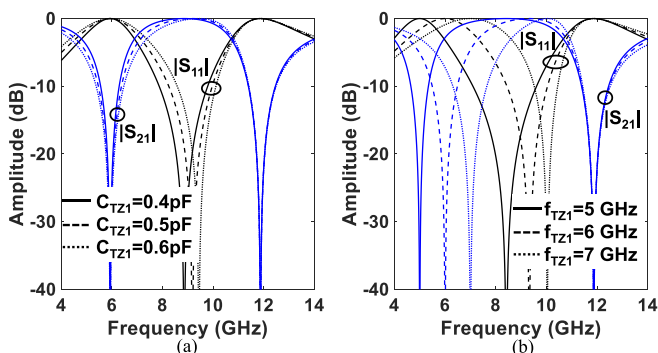

FIGURE 15. Design studies varying (a) C_{TZ1}, but keeping the TZ_2 resonant frequency constant and (b) the resonant frequency of the first TZ (f_{TZ1}).

FIGURE 16. Circuit-simulated S-parameters and examples of higher order FSQC circuits. (a) Three-pole/two-TZ FSQC using one passive resonator, one TZ generation cell, and one NRR per path. (b) Three-pole/four TZ FSQC using two TZ generation cells and one NRR per path. (c) Three-pole/two-TZ FSQC using one TZ generation cell and two NRRs per path.

direction. In order to increase the frequency selectivity and the out-of-band isolation of the FSQC, a TZ generation cell can be placed at the input port as shown in the conceptual diagram in Fig. 13(b) and the circuit simulated response in Fig. 13(c).

The TZ generation cell is comprised of two series LC resonators that are cascaded in parallel for size compactness. In this arrangement, they create two TZs at their respective resonant frequency and a pole at the average of the two resonant frequencies; an example of this is demonstrated in Fig. 14. Various design aspects can be considered, including the resonant frequency and the 3-dB rejection BW of the TZs; these considerations are provided in Fig. 15. In particular, the location of the pole can be altered by changing the 3dB rejection BW of the TZ (see Fig. 15(a)). Furthermore, the location of the pole can be altered by changing the resonant frequency of the TZs to either create a symmetric or an asymmetric response (see Fig. 15(b)).

When comparing the one-pole type FSQC to the two-pole/two-TZ type FSQC, the latter demonstrates higher selectivity, while the IS, IL and size are comparable to the one- pole design. The order, IS, and frequency selectivity of the two-pole/two-TZ FSQC could be increased if additional resonator types were added to the design. Examples of this are provided in Fig. 16, where either a passive resonator (Fig. 16(a)), or a TZ generation cell is added to the input port
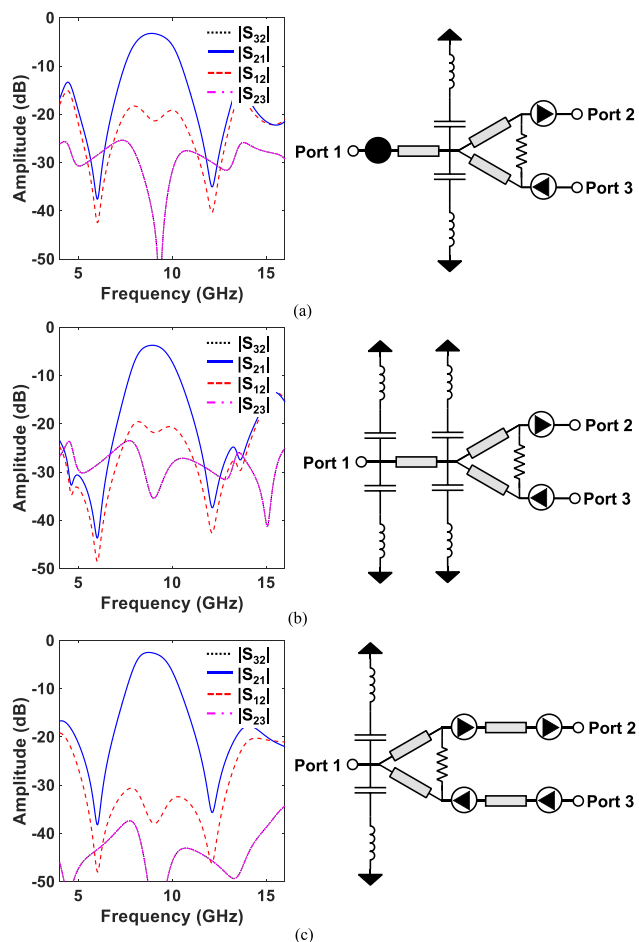
(see Fig. 16(b)), or additional NRRs are added to the output ports (see Fig. 16(c)).

As it can be seen in Fig. 16(a), the passive resonator increases the frequency selectivity of the FSQC, resulting in a three-pole/two-TZ FSQC, however, the IS and out-of-band response are the same as the two-pole/two-TZ FSQC. When a TZ generation cell is added to the input (Fig. 16(b)), the FQSC exhibits a three-pole/four-TZ response. In this instance, the second TZ generation cell can either be designed symmetrically or asymmetrically. An asymmetrically designed TZ generation cell is provided in Fig. 16(b). When compared to the two-pole/two-TZ FSQC, the out-of-band isolation and frequency selectivity are increased. In order to increase the isolation and frequency selectivity, NRRs can be added to the output ports as seen in the example in Fig. 16(c). In all of these examples, additional inverters had to be placed between the resonators, thus increasing the overall size of the FSQC.

In order to practically realize the FSQCs using the commercially available GaAs process, the layout for the two-pole/two-TZ FSQC in Fig. 17 is designed. The NRRs are
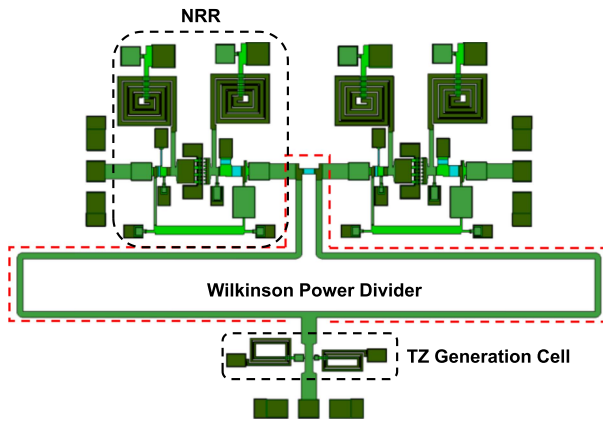
FIGURE 17. Layout of the two-pole/two-TZ FSQC with the NRR circled in black, the wilkinson power divider circled in red, and the TZ generation cell circled in black.

FIGURE 18. Photograph of the NRR based on the circuit schematic in Fig. 1. The transistor-based path is circled in blue.

made using the circuit and CRD described in Section II-A and Section II-B, however they are biased at $V_D = 2V$, $V_G = 0.85V$ ($P_{DC} = 284.6$ mW since two NRRs are used). The Wilkinson power divider is designed using quarter wavelength long TLs at X-band and the TZ generation cell for the two-pole/two-TZ FSQC is implemented using lumped elements for size compactness. The quality factor (Q) for the lower and upper TZ are 20.3 and 24.1, respectively.

III. EXPERIMENTAL VALIDATION

To evaluate the validity of the FSI/FSQC concepts, four proto-types were designed, manufactured, and measured at X-band using the WIN Semiconductor MMIC GaAs process, which consists of three metal layers (Metal 1, Metal 2, and ground), using circuit and full-wave electromagnetic (EM) analysis in AWR, Cadence. They include: i) a non-reciprocal resonator, ii) a two-resonator FSI, iii) a five-resonator FSI, and iv) a two-pole/two-TZ FSQC.

A. NON-RECIPROCAL RESONATOR

The NRR was designed using as a basis the circuit in Fig. 1 and the layout in Fig. 5, as shown in in Fig. 18. It was de-signed to enable gain (8-finger pHEMT transistor biased at $V_{DD} = 2V$, and $V_G = 0.8V$) in the forward direction and a TZ in the reverse direction at the operating frequency. The transistor-based path, including the lumped elements at the gate and the drain are circled in blue, while the TL connect-ing the gate and the drain is comprised of a distributed TL that is capacitively-loaded. A blocking capacitor is added to the TL to prevent biasing leakage and the bias lines include high-inductance inductors for size compactness.

When biased at $V_{DD} = 2V$ and $V_G = 0.8V$, the de-vice is turned on and provides a non-reciprocal response. A comparison between the EM-simulated and RF-measured S-parameters is provided in Fig. 19(a). As it can be seen, the measurements are in fair agreement. While the NRR was designed to have 1.2 dB of gain and 25.5 dB of IS, the
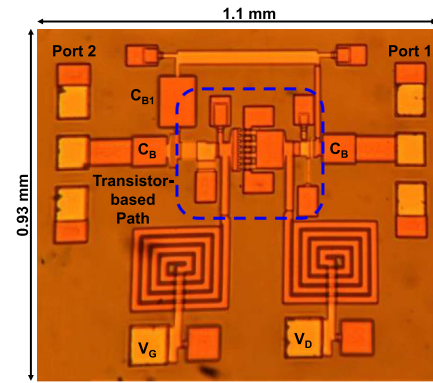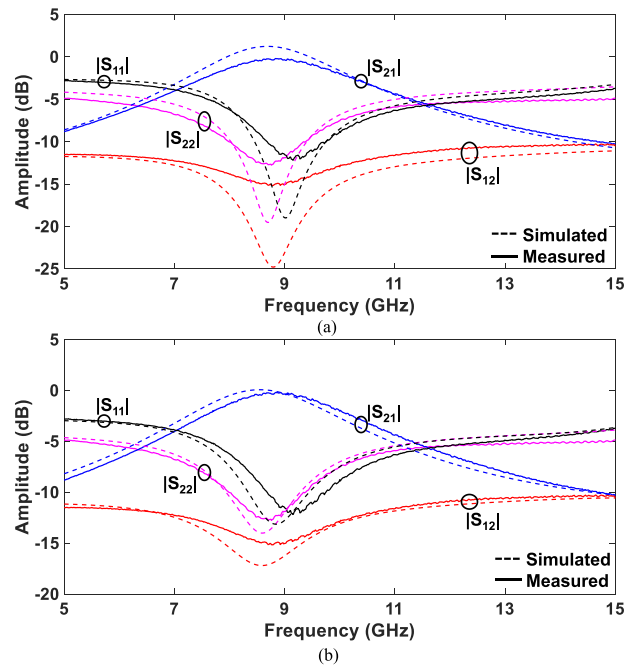

FIGURE 19. A comparison between the EM-simulated and RF-measured S-parameters for the NRR in Fig. 18. (a) Before process variation is considered. (b) After process variation is considered.

measurements result in IL of 0.2 dB and IS of 14.8 dB. The variation between the simulated and measured results are due to the variances in the MMIC process. When altering the lumped element values up to 5%, the measured results line up well with the simulated response thus successfully vali-dating the proposed concept; this is provided in Fig. 19(b). The measured results are summarized as follows: $f_{cen} = 8.8$ GHz, 36.2% FBW, $|S_{21}| = -0.2$ dB, maximum in-band IS = 14.9 dB, and minimum in-band IS = 8.9 dB. IS is defined by $|S_{21}|-|S_{12}|$ (i.e., directivity). Fig. 20 provides the NRR perfor-mance in terms of P_{1dB} and IIP_3/OIP_3 which are summarized as follows: $P_{1dB} = 15.5$ dBm, $IIP_3 = 18.4$ dBm, and $OIP_3 = 18.1$ dBm.
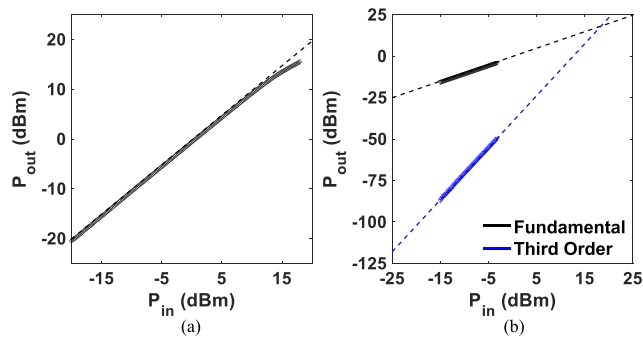
FIGURE 20. Measured (a) P_{1dB} and (b) IIP_3 and OIP_3 characterization for the NRR in Fig. 18.
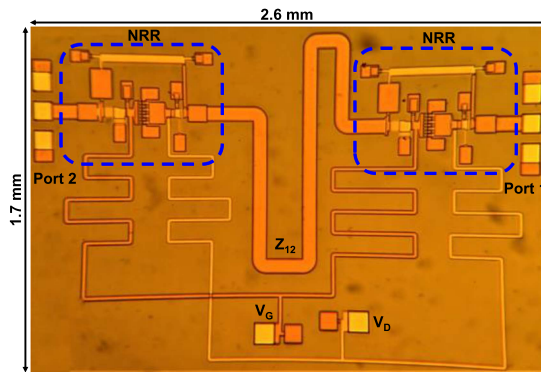

FIGURE 21. Photograph of the two-resonator FSI based on the FSI in Fig. 8. The NRRs are circled in blue.

B. TWO-RESONATOR FSI

To validate the two-resonator FSI in Fig. 8, a prototype was designed, manufactured and measured. It is comprised of two NRRs that are coupled through a quarter-wavelength-long TL. A photograph of the prototype is provided in Fig. 21 with the NRR circled in blue. Unlike the NRR prototype in Fig. 18, the two-resonator FSI has different biasing. The biasing combines the two gates together and the two drains together through TLs (added on a different metal layer), thus requiring a single bias point for the gates and a single bias point for the drains. The TLs are high impedance quarter-wavelength long at f_{cen}.

Considering the variances in the manufacturing process, a comparison of the EM-simulated results and RF-measured S-parameters for the two-resonator FSI prototype is provided in Fig. 22. The RF-measured performance for the prototype is summarized as follows: f_{cen} = 8.9 GHz, 18.7% FBW, $|S_{21}|$ = +0.3 dB, maximum in-band IS = 31.7 dB, and minimum in-band IS = 25.1 dB. Furthermore, as shown in Fig. 23 the two-resonator FSI exhibits P_{1dB} = 10.2 dBm, IIP_3 = 17.3 dBm, and OIP_3 = 17.2 dBm.

C. FIVE-RESONATOR FSI

To further increase the order and frequency selectivity of the FSI, a five-resonator prototype was designed, manufactured, and measured at X-band. As shown in Fig. 24, it is based
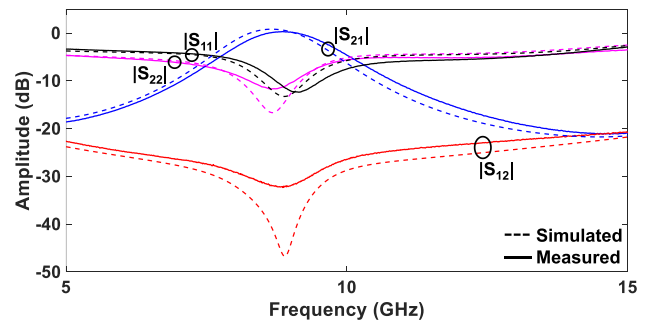

FIGURE 22. Comparison of the EM-simulated and RF-measured S-parameters for the two-resonator FSI in Fig. 21.
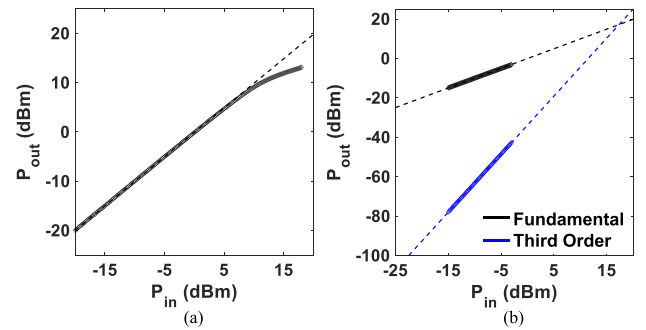
FIGURE 23. Measured (a) P_{1dB} and (b) IIP_3 and OIP_3 characterization for the two-resonator FSI in Fig. 21.
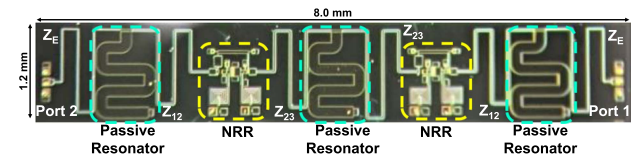
FIGURE 24. Photograph of the five-resonator FSI based on the CRD in Fig. 9.

on the circuit schematic in Fig. 9, with two NRRs (circled in yellow) and three passive resonators (circled in cyan). Quarter-wavelength-long TLs were used for the inverters and the passive resonators were shorted 90° stubs. A comparison of the simulated and measured results is provided in Fig. 25 showing good agreement, thus validating the proposed concept. The FSI performance is summarized as follows: f_{cen} = 8.6 GHz, 15.6% FBW, $|S_{21}|$ = -1.9 dB, maximum in-band IS = 30.6 dB, minimum in-band IS = 26.6 dB, P_{1dB} = 18.0 dBm, IIP_3 = 20.4 dBm, and OIP_3 = 17.2 dBm.

D. TWO POLE/TWO-TZ FSQC

The NRR concept was further expanded to the realization of FSQCs as shown in the photo in Fig. 26(a). It is based on the two-pole/two-TZ FSQC design in Fig. 13 and is comprised of a Wilkinson power divider, two NRRs (circled in blue), and a TZ generation cell (circled in black). Its performance is provided in Fig. 26(b) and is summarized as follows: f_{cen}

FIGURE 25. A comparison the EM-simulated and RF-measured S-parameters for the five-resonator FSI in Fig. 24.

FIGURE 27. Measured (a) P_{1dB} and (b) IIP_3 and OIP_3 characterization for the two-pole/two-TZ FSQC in Fig. 26.
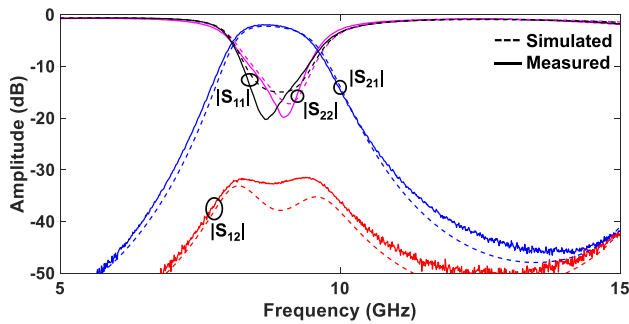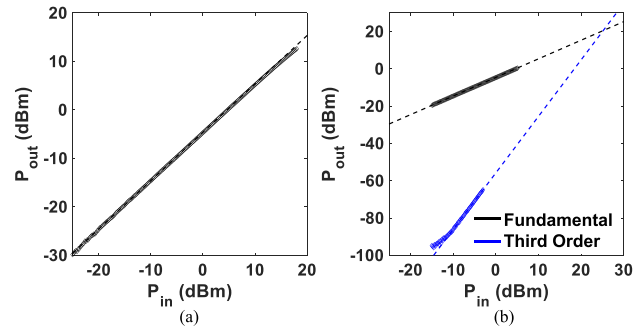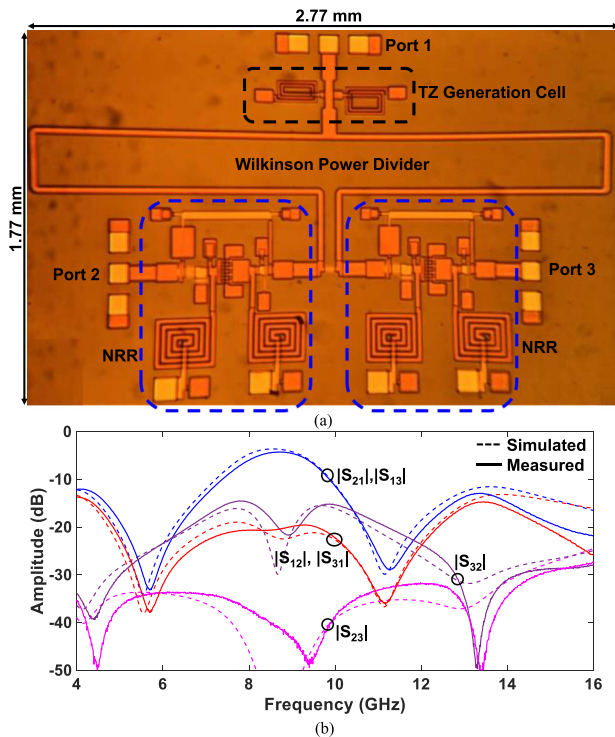

FIGURE 26. (a) Photograph of the two-pole/two-TZ FSQC based on the schematic in Fig. 13(b). Black circle: TZ generation cell, Blue circle: NRR. (b) EM-simulated and RF-measured S-parameters comparison for the prototype in (a).

= 8.7 GHz, 22.0% FBW, $|S_{21}| = -4.3$ dB, $|S_{31}|$ IS = 16.2 dB, $|S_{32}|$ IS = 15.9 dB, and $|S_{23}|$ IS = 36.9 dB. While not all of the S-parameters are provided, the measured results line up well with the simulated results, thus successfully validating the concept. Its out-of-band performance can be improved by increasing the filter order, i.e., by adding passive resonators or NRRs. Its measured non-linear performance parameters are provided in Fig. 27 and summarized as follows: $P_{1dB} > 18$ dBm, $IIP_3 = 25.2$ dBm, and $OIP_3 = 20.5$ dBm. It is worth noting that the P_{1dB} is higher than 18 dBm, however our equipment was unable to measure at a higher input power level.

E. COMPARISON WITH THE STATE-OF-ART

A comparison of the proposed MMIC FSIs with other state-of-the-art (SOA) FSIs and IC-based isolators is provided in Table 3. When compared to other GaAs MMIC FSIs [43], the FSI concept has been validated for higher order transfer functions (5 poles vs. 3 poles in [43]) while it exhibits comparable IS. Overall, this work proves to be more modular and scalable to higher order transfer functions, different levels of gain and IS by incorporating different resonator types (i.e., passive resonators, NRRs, and TZ generation cells). When compared to STM-based FSIs, the devised FSIs have been demonstrated at a significantly higher frequencies (8.8 GHz versus <1.2 GHz in [32], [33], [34], [35], [36], [37]). Furthermore, they have lower IL (<2 dB versus 3.7 dB in [32]), and higher order transfer functions. While the transistor-based FSIs in [42] provide higher gain and IS, they are significantly larger in size and operate at a lower operating frequency. Moreover, when compared to the other integrated isolator components in [16], [17], [18], [19], they exhibit comparable IS and IL, however the proposed approach combines the functions of the RF isolator and BPF into a single component, thus reducing the overall size of the device. When compared to the transistor-based isolator in [19], the proposed approach provides better linearity (18.4 vs. 0.7 dBm). When directly compared to the GaAs integrated FSIs or isolators, the proposed approach provides better performance with respect to IL and the number of resonators and TZs incorporated into its design.

A comparison of the proposed MMIC FSQC with SOA FSQCs and active circulators is provided Table 4. As it can be seen, there are only two demonstrations of co-designed FSQCs [31], [44]. The proposed topology results in a significantly smaller size (0.094λ by 0.084λ vs. 0.48λ by 0.34λ in [44]) and higher operating frequency than the FSQCs in [31] and [44]. The proposed FSQC results in better matching at the RF ports than the active circulators reported in [23], [24], [25], [28]. In relation to the quasi-circulator in [16], the devised FSQC results in better IS levels (>16 dB). When looking at the P_{1dB}, this approach provides the best performance (P_{1dB} >18 dBm vs. <−2.1 dBm in [25], [29], and [30]). In addition, the proposed FSQC provides higher IIP_3 (25.2 dBm vs 1.2 in [29]). When compared to the circulators in [45], [46], [47],

TABLE 3. Comparison of the Proposed FSIs With State-of-Art Isolators and NBPFs

Ref.	Component & approach	Process	f_{cen} (GHz)	FBW (%)	$|S_{21}|$ (dB)	IS (dB)	Filtering	Res./TZs	P_{DC} (mW)	P_{1dB} (dBm)	IIP$_3$/OIP$_3$ (dBm)	Size ($\lambda \times \lambda$)
[16]	Transistor-based isolator, MMIC	GaAs	9.4	N/A	9.3	27.7	No	0/0	68.75	N/A	N/A	0.054 x 0.052
[17]	Transistor-based isolator, CMOS	CMOS	24	N/A	-1.8	36.8	No	0/0	3.6	N/A	N/A	0.053 x 0.035
[18]	Transistor-based isolator, MMIC	GaAs	1.4	N/A	-2.5	31	No	0/0	N/A	N/A	N/A	0.004 x 0.003
[19]	Transistor-based isolator, SiGe	SiGe	5.5	N/A	-2	35	No	0/0	2.6	N/A	0.7/N/A	0.012 x 0.008
[32]	STM NBPF, hybrid PCB	N/A	0.14	19.2	-3.7	52.8	Yes	3/0	0	N/A	N/A	N/A
[33]	STM NBPF, hybrid PCB	N/A	1	6.3	-5.5	6.2	Yes	2/0	0	N/A	N/A	0.069 x 0.061
[34]	STM NBPF, hybrid PCB	N/A	1.175	1.7	-4.5	28	Yes	3/0	0	N/A	N/A	N/A
[42]	Transistor-based NBPF, PCB	N/A	2.3	10.7	5.8	59.7	Yes	7/4	N/A	N/A	N/A	0.434 x 1.03
[43]	Transistor-based NBPF, MMIC	GaAs	9.0	8.1	2.8	28.8	Yes	3/4	N/A	N/A	N/A	0.072 x 0.055
This work	NRR, MMIC	GaAs	8.8	36.2	-0.2	14.9	Yes	1/0	114.3	15.5	18.4/18.1	0.027 x 0.032
	Two-Resonator FSI, MMIC	GaAs	8.9	18.7	0.3	31.7	Yes	2/0	228.6	10.2	17.3/17.2	0.050 x 0.077
	Five-Resonator FSI, MMIC	GaAs	8.6	15.6	-1.9	30.6	Yes	5/0	228.6	8.0	20.4/17.2	0.034 x 0.233

TABLE 4. Comparison of the Proposed FSQC With State-of-Art FSQCs and Circulators

Ref.	Component & approach	Process	f_{cen} (GHz)	FBW (%)	$|S_{21}|$ (dB)	IS (dB)	Filtering	Res./TZs	P_{DC} (mW)	P_{1dB} (dBm)	IIP$_3$/OIP$_3$ (dBm)	Size ($\lambda \times \lambda$)
[20]	Transistor-based quasi-circulator, CMOS	CMOS	24	N/A	-5.7	20	No	0/0	7.2	9.5	N/A	0.104 x 0.044
[21]	Transistor-based quasi-circulator, MMIC	GaAs	11.5	N/A	-4.5	35	No	0/0	N/A	N/A	N/A/34.6	0.153 x 0.153
[23]	Transistor-based quasi-circulator, CMOS	CMOS	5.55	N/A	-6	18	No	0/0	31.6	N/A	N/A	0.013 x 0.105
[24]	Transistor-based quasi-circulator, CMOS	CMOS	30	N/A	-5	12	No	0/0	15	N/A	-7/N/A	0.057 x 0.064
[25]	Transistor-based quasi-circulator, CMOS	CMOS	3.8	N/A	-9	27	No	0/0	12.8	-2.14	N/A	0.007 x 0.008
[29]	Transistor-based quasi-circulator, CMOS	CMOS	2.1	N/A	2	24	No	0/0	86	-6.4	1.2/3.4	N/A
[30]	Amplifier-based quasi-circulator, CMOS	CMOS	9.9	N/A	7	17.3	No	0/0	18.6	-6.1	N/A	N/A
[31]	Ferrite-based frequency selective circulator	N/A	3	9.7-17.7	-2.7 to -4.5	11.5 to 33.1	Yes	2/4	0	N/A	N/A	N/A
[44]	Transistor-based FSQC, PCB	N/A	2.4	N/A	-0.5	26.8	Yes	2/0	132	N/A	N/A	0.48 x 0.34
[45]	Transistor-based quasi-circulator, PCB	N/A	3.22	N/A	4.3	19.3	No	0/0	N/A	21.7	17.7/N/A	0.455 x 0.514
[46]	N-path capacitor	CMOS	0.725	N/A	-3.1	11	No	0/0	N/A	N/A	25/N/A	0.0024 x 0.0024
[47]	Switched reflecting T-line gyrator	CMOS	1	N/A	-2.5	~45	No	0/0	104	17.3	36.5/N/A	0.0075 x 0.0136
[48]	STM-based circulator, PCB	N/A	1	N/A	2	23	No	0/0	N/A	28	31/N/A	0.036 x 0.043
This work	Two-Pole/Two-TZs FSQC, MMIC	GaAs	8.7	22	-4.3	15.9	Yes	2/2	284.6	> 18	25.2/20.5	0.053 x 0.082

[48], the proposed approach operates at a higher frequency (8.7 GHz vs <3.2 GHz) and incorporates filtering capabilities. Whereas the configurations in [45], [46], [47], [48], may demonstrate a somewhat frequency dependent response, their selectivity is poor and doesn't really makes them comparable to what is expected by a filter. None of these designs can be scaled to high order BPF response which is a major contribution of this work. As such, when using the approaches in [45], [46], [47], [48], the RF front-end would exhibit larger physical size as it would require to cascade additional filters in each

branch of the RF circulator. The proposed FSQC has better P_{1dB} than the design in [47] and better IIP$_3$ than the design in [45], [46]. Furthermore, the FSQC presented in this work results in better IS than the design in [46]. Lastly, this is the first demonstration of a fully-integrated frequency selective circulator with more than two poles.

IV. CONCLUSION

This manuscript presented the operating principles and practical implementation aspects of a new class of multi-functional MMIC RF components that exhibit the combined function of a BPF and an RF isolator/circulator. The proposed FSIs are based on cascading in series NRRs with passive resonators to increase the frequency selectivity of the RF component. The operating principles of the FSI concept and its extension to high order transfer functions were uniquely presented through circuit-based and CRD-synthesized examples allowing for the scalability of the proposed concept to high order and advanced transfer functions. The proposed FSQC is based on the combination of a Wilkinson power divider, a TZ generation cell, and NRRs to create a two-pole/two-TZ non-reciprocal transfer function. For proof-of-concept validation purposes, four prototypes were designed and measured at X-band using the WIN Semiconductor GaAs process. They include: i) a NRR ii) a two-resonator FSI, iii) a five-resonator FSI, and iv) a two-pole/two-TZ FSQC.

ACKNOWLEDGMENT

REFERENCES

[1] A. Parsa, "Fast moving target detection in sea clutter using non-coherent X-band radar," in *Proc. IEEE Radar Conf.*, 2014, pp. 1155–1158.

[2] R. Baqué et al., "Ultra-high resolution and long range X-band airborne SAR system," in *Proc. Int. Conf. Radar*, 2018, pp. 1–6.

[3] V. Ghanvat, A. Heddallikar, and A. Rameshbabu, "Design and development of rugged wide beam-width miniaturized bi-static patch antenna for X-band FMCW system," in *Proc. Int. Conf. Innov. Trends Adv. Eng. Technol.*, 2019, pp. 43–46.

[4] S. Singh and J. Kumar, "Miniaturized triband circular patch antenna for X band, Ku band and K band applications," in *Proc. 9th Int. Conf. Syst. Model. Adv. Res. Trends*, 2020, pp. 355–359.

[5] K. Borah and N. S. Bhattacharyya, "Miniaturized patch antennas on magnetodielectric substrate for X band communications," in *Proc. Int. Conf. Devices Commun.*, 2011, pp. 1–3.

[6] M. L., H. N., and S. K., "Compact X band MMIC low noise amplifier for radar applications," in *Proc. IEEE Int. Conf. Innov. Technol.*, 2020, pp. 1–4.

[7] J. Kamioka et al., "A low-cost 30-W class X-band GaN-on-Si MMIC power amplifier with a GaAs MMIC output matching circuit," in *Proc. 13th Eur. Microw. Integr. Circuits Conf.*, 2018, pp. 93–96.

[8] T. Paul, M. Harinath, and S. K. Garg, "X-band self biased MMIC amplifier using 250nm GaAs pHEMT process," in *Proc. IEEE MTT-S Int. Microw. RF Conf.*, 2017, pp. 1–5.

[9] X. Li, E. Li, and G. Guo, "Design of X-band H-plane waveguide Y-junction circulator," in *Proc. Int. Workshop Microw. Millimeter Wave Circuits Syst. Technol.*, 2012, pp. 1–4.

[10] M. F. Farooqui, A. Nafe, and A. Shamim, "Inkjet printed ferrite-filled rectangular waveguide X-band isolator," in *Proc. IEEE MTT-S Int. Microw. Symp.*, 2014, pp. 1–4.

[11] S. Yang, D. Vincent, J. R. Bray, and L. Roy, "Ferrite LTCC edge-guided circulator," in *Proc. 44th Eur. Microw. Conf.*, 2014, pp. 1540–1543.

[12] H. Dong, J. R. Smith, and J. L. Young, "A wide-band, high isolation UHF lumped-element ferrite circulator," *IEEE Microw. Wireless Compon. Lett.*, vol. 23, no. 6, pp. 294–296, Jun. 2013.

[13] W. Marynowski, "Integrated broadband edge-guided mode isolator with antiparallel biasing of the ferrite slabs," *IEEE Microw. Wireless Compon. Lett.*, vol. 28, no. 5, pp. 392–394, May 2018.

[14] L. Nan, K. Mouthaan, Y. Xiong, J. Shi, S. C. Rustagi, and B. Ooi, "Design of 60- and 77-GHz narrow-bandpass filters in CMOS technology," *IEEE Trans. Circuits Syst. II, Exp. Briefs*, vol. 55, no. 8, pp. 738–742, Aug. 2008.

[15] L.-K. Yeh, C.-Y. Chen, and H.-R. Chuang, "A millimeter-wave CPW CMOS on-chip bandpass filter using conductor-backed resonators," *IEEE Electron. Device Lett.*, vol. 31, no. 5, pp. 399–401, May 2010.

[16] A. Ashley, G. Lasser, Z. Popovic, A. Madanayake, and D. Psychogiou, "MMIC GaAs X-band isolator with enhanced power transmission," in *Proc. Integr. Circuits RF Syst.*, 2021, pp. 22–24.

[17] J.-F. Chang, J.-C. Kao, Y.-H. Lin, and H. Wang, "A 24-GHz fully integrated isolator with high isolation in standard RF 180-nm CMOS technology," in *Proc. IEEE MTT-S Int. Microw. Symp.*, 2014, pp. 1–3.

[18] M. F. Cordoba-Erazo and T. M. Weller, "A 1.4 GHz MMIC active isolator for integrated wireless systems applications," in *Proc. WAMICON*, 2014, pp. 1–3.

[19] J. Lee, J. D. Cressler, and A. J. Joseph, "A 5-6 GHz SiGe HBT monolithic active isolator for improving reverse isolation in wireless systems," *IEEE Microw. Wireless Compon. Lett.*, vol. 15, no. 4, pp. 220–222, Apr. 2005.

[20] J.-F. Chang, J.-C. Kao, Y.-H. Lin, and H. Wang, "Design and analysis of 24-GHz active isolator and quasi-circulator," *IEEE Trans. Microw. Theory Techn.*, vol. 63, no. 8, pp. 2638–2649, Aug. 2015.

[21] S. K. Cheung, T. P. Halloran, W. H. Weedon, and C. P. Caldwell, "MMIC-based quadrature hybrid quasi-circulators for simultaneous transmit and receive," *IEEE Trans. Microw. Theory Techn.*, vol. 58, no. 3, pp. 489–497, Mar. 2010.

[22] L. Marzall, S. Verploegh, T. Cappello, M. Roberg, and Z. Popović, "Active MMIC circulator performance in a phased-array-like environment," in *Proc. 50th Eur. Microw. Conf.*, 2021, pp. 1186–1189.

[23] S.-C. Shin, J.-Y. Huang, K.-Y. Lin, and H. Wang, "A 1.5–9.6 GHz monolithic active quasi-circulator in 0.18 μm CMOS technology," *IEEE Microw. Wireless Compon. Lett.*, vol. 18, no. 12, pp. 797–799, Dec. 2008.

[24] C.-H. Chang, Y.-T. Lo, and J.-F. Kiang, "A 30 GHz active quasi-circulator with current-reuse technique in 0.18 μm CMOS technology," *IEEE Microw. Wireless Compon. Lett.*, vol. 20, no. 12, pp. 693–695, Dec. 2010.

[25] B. Tang, J. Xu, and L. Geng, "Integrated active quasi-circulator with 27 dB isolation and 0.8–6.8GHz wideband by using feedback technique," in *Proc. IEEE MTT-S Int. Wireless Symp.*, 2018, pp. 1–4.

[26] M. Porranzl, C. Wagner, H. Jaeger, and A. Stelzer, "An active quasi-circulator for 77 GHz automotive FMCW radar systems in SiGe technology," *IEEE Microw. Wireless Compon. Lett.*, vol. 25, no. 5, pp. 313–315, May 2015.

[27] D. Ghosh and G. Kumar, "A broadband active quasi circulator for UHF and L band applications," *IEEE Microw. Wireless Compon. Lett.*, vol. 26, no. 8, pp. 601–603, Aug. 2016.

[28] A. Gasmi, B. Huyart, E. Bergeault, and L. Jallet, "MMIC quasi-circulator with low noise and medium power," in *IEEE MTT-S Int. Microw. Symp. Dig.*, vol. 3, 1996, pp. 1233–1236.

[29] Y. Zheng and C. E. Saavedra, "Active quasi-circulator MMIC using OTAs," *IEEE Microw. Wireless Compon. Lett.*, vol. 19, no. 4, pp. 218–220, Apr. 2009.

[30] S. Wang, C.-H. Lee, and Y.-B. Wu, "Fully integrated 10-GHz active circulator and quasi-circulator using bridged-T networks in standard CMOS," *IEEE Trans. Very Large Scale Integr. (VLSI) Syst.*, vol. 24, no. 10, pp. 3184–3192, Oct. 2016.

[31] A. Ashley and D. Psychogiou, "RF co-designed bandpass filter/circulator (BPFC) with tunable center frequency, bandwidth, and out-of-band isolation," *IEEE Microw. Wireless Compon. Lett.*, vol. 21, no. 7, pp. 845–848, Jul. 2021.

[32] D. Simpson and D. Psychogiou, "Magnet-less non-reciprocal bandpass filters with tunable center frequency," in *Proc. 49th Eur. Microw. Conf.*, 2019, pp. 460–463.

[33] X. Wu, M. Nafe, A. A. Melcón, J. Sebastián Gómez-Díaz, and X. Liu, "A non-reciprocal microstrip bandpass filter based on spatio-temporal modulation," in *Proc. IEEE MTT-S Int. Microw. Symp.*, 2019, pp. 9–12.

[34] M. Pirro et al., "Novel topology for a non-reciprocal MEMS filter," in *Proc. IEEE Int. Ultrason. Symp.*, 2018, pp. 1–3.

[35] M. Pirro, C. Cassella, G. Michetti, and M. Rinaldi, "Low loss non-reciprocal filter for miniaturized RF-front-end platforms," in *Proc. Joint Conf. IEEE Int. Freq. Control Symp. Eur. Freq. Time Forum*, 2019, pp. 1–3.

[36] D. Simpson and D. Psychogiou, "Fully-reconfigurable non-reciprocal bandpass filters," in *Proc. IEEE/MTT-S Int. Microw. Symp.*, 2020, pp. 807–810.

[37] X. Wu, M. Nafe, A. Á. Melcón, J. S. Gómez-Díaz, and X. Liu, "Frequency tunable non-reciprocal bandpass filter using time-modulated microstrip λg/2 resonators," *IEEE Trans. Circuits Syst., II, Exp. Briefs*, vol. 68, no. 2, pp. 667–671, Feb. 2021.

[38] M. M. Torunbalci, T. J. Odelberg, S. Sridaran, R. C. Ruby, and S. A. Bhave, "An FBAR circulator," *IEEE Microw. Wireless Compon. Lett.*, vol. 28, no. 5, pp. 395–397, May 2018.

[39] Y. Yu et al., "Highly-linear magnet-free microelectromechanical circulators," *J. Microelectromech. Syst.*, vol. 28, no. 6, pp. 933–940, Dec. 2019.

[40] A. Alvarez-Melcon, X. Wu, J. Zang, X. Liu, and J. S. Gomez-Diaz, "Coupling matrix representation of nonreciprocal filters based on time-modulated resonators," *IEEE Trans. Microw. Theory Techn.*, vol. 67, no. 12, pp. 4751–4763, Dec. 2019.

[41] C. Cassella et al., "Radio frequency angular momentum biased quasi-LTI nonreciprocal acoustic filters," *IEEE Trans. Ultrason., Ferroelect., Freq. Control*, vol. 66, no. 11, pp. 1814–1825, Nov. 2019.

[42] A. Ashley and D. Psychogiou, "RF co-designed bandpass filters/isolators using nonreciprocal resonant stages and microwave resonators," *IEEE Trans. Microw. Theory Techn.*, vol. 69, no. 4, pp. 2178–2190, Apr. 2021.

[43] A. Ashley and D. Psychogiou, "X-band quasi-elliptic non-reciprocal bandpass filters (NBPFs)," *IEEE Trans. Microw. Theory Techn.*, vol. 69, no. 7, pp. 3255–3263, Jul. 2021.

[44] A. Ashley and D. Psychogiou, "Co-designed quasi-circulator and bandpass filter," in *Proc. 50th Eur. Microw. Conf.*, 2021, pp. 890–893.

[45] Z. Deng, H. Qian, and X. Luo, "Tunable quasi-circulator based on a compact fully-reconfigurable 180° hybrid for full-duplex transceivers," *IEEE Trans. Circuits Syst. I, Reg. Papers*, vol. 66, no. 8, pp. 2949–2962, Aug. 2019.

[46] S. Jain, A. Agrawal, M. Johnson, and A. Natarajan, "A 0.55-to-0.9 GHz 2.7 dB NF full-duplex hybrid-coupler circulator with 56 MHz 40 dB TX SI suppression," in *Proc. IEEE Int. Solid-State Circuits Conf.*, 2018, pp. 400–402.

[47] A. Nagulu, T. Chen, G. Zussman, and H. Krishnaswamy, "Multi-watt, 1-GHz CMOS circulator based on switched-capacitor clock boosting," *IEEE J. Solid-State Circuits*, vol. 55, no. 12, pp. 3308–3321, Dec. 2020.

[48] A. Kord, D. L. Sounas, and A. Alù, "Pseudo-linear time-invariant magnetless circulators based on differential spatiotemporal modulation of resonant junctions," *IEEE Trans. Microw. Theory Techn.*, vol. 66, no. 6, pp. 2731–2745, Jun. 2018.

[49] A. Kord, M. Tymchenko, D. L. Sounas, H. Krishnaswamy, and A. Alù, "CMOS integrated magnetless circulators based on spatiotemporal modulation angular-momentum biasing," *IEEE Trans. Microw. Theory Techn.*, vol. 67, no. 7, pp. 2649–2662, Jul. 2019.

[50] A. Ruffino, Y. Peng, F. Sebastiano, M. Babaie, and E. Charbon, "A 6.5-GHz cryogenic all-pass filter circulator in 40-nm CMOS for quantum computing applications," in *Proc. IEEE Radio Freq. Integr. Circuits Symp.*, 2019, pp. 107–110.

[51] T. Dinc and H. Krishnaswamy, "17.2 A 28GHz magnetic-free non-reciprocal passive CMOS circulator based on spatio-temporal conductance modulation," in *Proc. IEEE Int. Solid-State Circuits Conf.*, 2017, pp. 294–295.

[52] A. Nagulu and H. Krishnaswamy, "28.5 non-magnetic 60GHz SOI CMOS circulator based on loss/dispersion-engineered switched bandpass filters," in *Proc. IEEE Int. Solid- State Circuits Conf.*, 2019, pp. 446–448.

ANDREA ASHLEY (Member, IEEE) was born in Tulsa, OK, USA, in 1992. She received the B.S. degree in mechanical and electrical engineering from Kettering University, Flint, MI, in 2014, and the M.S. degree in electrical engineering in 2019 from the University of Colorado Boulder, CO, USA, where she is currently working toward the Ph.D. degree in electrical engineering.

Her research interests include the design, characterization, and synthesis of reconfigurable microwave non-reciprocal RF filters and circulators.

She is a member of the IEEE Microwave Theory and Techniques Society and the Applied Computational Electromagnetics Society. She was the recipient of the 2018 National Defense Science and Engineering Graduate Fellowship, ECEE Gold Award for Research, 2018 EuMC Young Engineer Prize, and the University of Colorado's Dean's Graduate Assistantship.

DIMITRA PSYCHOGIOU (Senior Member, IEEE) received the Dipl.-Eng. degree in electrical and computer engineering from the University of Patras, Patras, Greece, in 2008, and the Ph.D. degree in electrical engineering from the Swiss Federal Institute of Technology, Zürich, Switzerland, in 2013. She is currently a Professor of electrical and electronic engineering with the University College Cork (UCC), Cork, Ireland; Head of the Advanced RF Technology Group with Tyndall National Institute, Cork, Ireland; and an SFI Research Professor.

Prior to joining UCC, she was a Senior Research Scientist with Purdue University, West Lafayette, IN, USA, and an Assistant Professor with the University of Colorado Boulder, Boulder, CO, USA. Her research interests include RF design and characterization of reconfigurable microwave and millimeter-wave passive, active components and antennas, RF MEMS, acoustic wave resonator-based filters, tunable filter synthesis, and additive manufacturing techniques for 3D antenna systems.

Prof. Psychogiou is a Senior Member of URSI and a member of the IEEE MTT-S Filters and Passive Components (MTT-5) and Microwave Control Materials and Devices (MTT-13) Committees. Furthermore, she is on the Technical Review Board for various IEEE and EuMA conferences and journals. Her research has been presented in more than 200 IEEE publications. She was the recipient of the 2021 Research Professorship Award from the Science Foundation Ireland, 2021 Roberto Sorrentino Prize from the European Microwave Association (EuMA), 2020 CAREER Award from the National Science Foundation (NSF), USA, 2020 URSI Young Scientist Award, and Junior Faculty Outstanding Research Award from UC Boulder. Prof. Psychogiou is the Chair of MTT-13 and the Secretary of USNC-URSI Commission D. She is an Associate Editor for IEEE MICROWAVE AND WIRELESS COMPONENTS LETTERS and the *International Journal of Microwave and Wireless Technologies*. She was an Associate Editor for the *IET Microwaves, Antennas & Propagation* journal.